PROCEEDINGS OF THE ROYAL SOCIETY A

Proc. R. Soc. A (2006) **462**, 2315–2330
doi:10.1098/rspa.2006.1688
Published online 8 March 2006

M_4C_3 precipitation in Fe–C–Mo–V steels and relationship to hydrogen trapping

By S. Yamasaki and H. K. D. H. Bhadeshia*

Department of Materials Science and Metallurgy, University of Cambridge, Pembroke Street, Cambridge CB2 3QZ, UK

Strong steels suffer from embrittlement due to dissolved hydrogen, a phenomenon which can be mitigated by trapping the hydrogen at carbide particles, where it is rendered benign. The precipitation and coarsening of plate-like M_4C_3 carbides, during the tempering of quaternary Fe–C–Mo–V martensitic steels, has been characterized both experimentally and by developing appropriate kinetic theory. The trapping capacity is found to peak when the carbides are about 10 nm in length, indicating a role of coherency strains in trapping hydrogen atoms via elastic interactions. This suggests a method for developing alloys which are better able to resist the detrimental effects of hydrogen.

Keywords: steel; precipitation kinetics; martensite; hydrogen trapping

1. Introduction

Alloy carbides have played an important role in the development of structural steels, including those which are microalloyed or secondary-hardened (Honeycombe & Bhadeshia 1995*a*,*b*; Gladman 1997). Less familiar is the exploitation of carbides as hydrogen-trapping sites, to enhance the resistance of strong steels to static fracture (Kushida *et al.* 1996; Ibaraki *et al.* 1998; Tarui & Yamasaki 2002). The trapping ability is thought to depend on many parameters, but the emphasis has been on particle size and number density.

We have, in the past, estimated the nucleation, growth and coarsening of V_4C_3 carbides, assuming local equilibrium, accounting for capillarity effects, and changes in the cementite which precedes the V_4C_3 (Yamasaki & Bhadeshia 2003). The purpose here was to study $(V,Mo,Fe,Mn)_4C_3$ in a more complex Fe–C–V–Mo quaternary system, where the lattice parameter of the carbide, and hence its coherency with the matrix, is a function of the V/Mo ratio. It has been reported that this mixed carbide can be better than pure V_4C_3 in its ability to capture hydrogen (Kosaka *et al.* 2004). Following convention, $(V,Mo,Fe,Mn)_4C_3$ is henceforth referred to as M_4C_3, with 'M' denoting metal atoms.

* Author for correspondence (hkdb@cus.cam.ac.uk).

Received 30 January 2006
Accepted 6 February 2006

© 2006 The Royal Society

Table 1. Chemical compositions (wt%).

	C	Si	Mn	Mo	V	Al	N
Steel A	0.10	<0.005	2.00	1.59	0.56	0.03	0.0044
Steel B	0.10	<0.005	2.00	0.40	0.56	0.03	0.0040
Steel C	0.10	<0.005	2.00	0.40	0.30	0.03	0.0041
base	0.10	<0.005	2.01	0.00	0.00	0.03	0.0056

2. Experimental work

Transmission electron microscopy (TEM) was used to assess carbide length, volume fraction, number density and chemical composition. The steels studied are listed in table 1. They were vacuum-melted as 10 kg ingots, heated at 1250 °C for 30 min in argon, hot-rolled to 12 mm thick plates and air-cooled. Specimens for heat treatment were machined to 3 and 8 mm diameter cylinders. After sealing in silica tubes under a partial pressure of argon (about 150 mm Hg), they were homogenized at 1250 °C for 50 h, since phase diagram calculations using MTDATA (NPL 2004) indicated that they would be fully austenitic above 1000 °C. MTDATA is a software which accesses a thermodynamic database (in our case SGTE database) to estimate the equilibrium compositions and phase fractions as a function of temperature and pressure, for a specified set of phases and species (Hack 1996).

After homogenization, the specimens were plunged into water and the silica tubes broken. They were re-sealed and tempered at 600 °C for time periods ranging from 0.5 to 1160 h, before finally quenching in water.

(*a*) *Sample preparation*

Thin foils were prepared using 250 μm thick and 3 mm diameter slices, which were ground using silicon carbide to approximately 50 μm thickness. Electropolishing was conducted using a twin jet electropolisher (Kelly & Nutting 1959) in 8% perchloric acid, 14% glycerol and 78% methanol solution at 15 °C, 50 V.

Single-stage carbon extraction replicas were prepared from metallographic samples etched in 4% nital, by depositing a 20–30 nm carbon layer, which was then scored with a sharp blade to partition it into 1 mm^2 squares. Electrolytic etching in a solution of 5% hydrochloric acid in methanol at 7.5 V allowed the carbon to be floated off on to copper grids.

(*b*) *TEM observations*

Figure 1 shows typical images from Steel A tempered for 30 and 560 h; the actual experiments covered a wider range of time periods. These pictures were taken from the [001] orientation of the matrix. Diffraction patterns from extraction replicas confirmed that the plate-shaped precipitates have a face-centred cubic lattice with almost the same lattice parameter as V_4C_3 (4.2 Å). M_4C_3 grows on the three equivalent $\{001\}_\alpha$ planes of the α-ferrite (Tanino 1988). In figure 1, what appear to be needles, are cross-sections of plates growing on the $\{001\}_\alpha$ plane parallel to the observation direction.

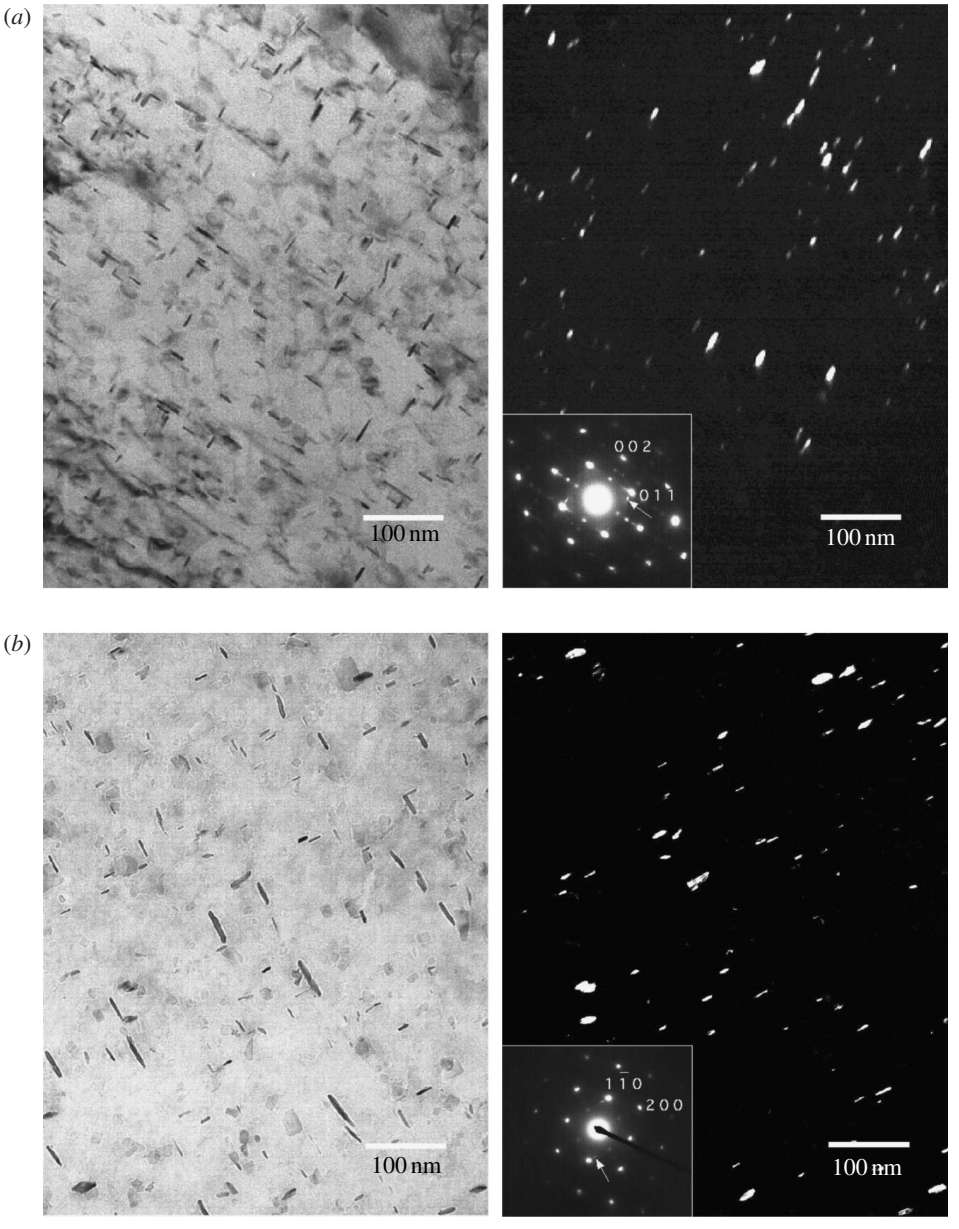

Figure 1. Transmission electron micrographs of Steel A tempered at 600 °C for (*a*) 30 h and (*b*) 560 h. The zone axis is $\langle 001 \rangle_\alpha$. Note that the carbides, which precipitate with their habit plane in the foil, appear as faint discs in the bright-field images. Each dark field image was taken using the diffraction spot identified by the arrow.

Precipitate compositions were estimated using energy dispersive X-ray spectroscopy on the carbon extraction replicas; the measured ratios of metallic elements are discussed later, but they indicated that the carbides are essentially $(V,Mo)_4C_3$ with the Mo/V ratio changing with the tempering time. The foil thicknesses were measured using grain boundary fringes and known extinction distances for the two-beam condition.

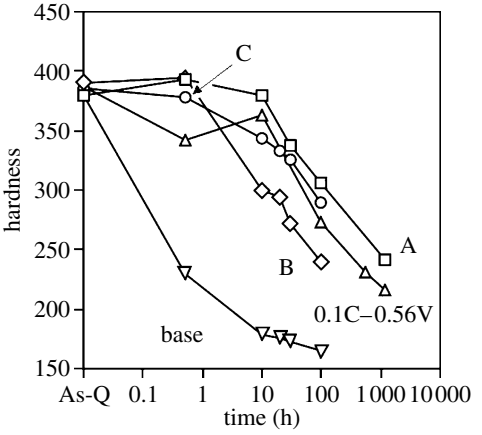

Figure 2. Relationship between hardness and tempering time at 600 °C.

M_4C_3 grows in the form of plates with an average aspect ratio of 5–6. The carbide size was measured for each sample from at least five different locations, each of which contained over 500 particles. The volume fraction was calculated using the product length$^2 \times$width for each carbide particle and the foil thickness.

(*c*) *Hardness measurements*

Vickers hardness measurements were made on metallographic samples with a load of 10 kg applied for 10 s. Five measurements were taken in each case. Figure 2 shows the data, with 'Q' denoting 'as-quenched'. Data from a previous study of 0.1C–2.0Mn–0.56V are included for comparison (Yamasaki & Bhadeshia 2003).

(*d*) *Hydrogen trapping measurements*

These were conducted on cylindrical samples 8 mm diameter, 7 mm length using a programmed-temperature gas chromatograph (Asahi *et al.* 2002). The evolution rate of diffusible hydrogen responsible for the embrittlement of steel peaks at 100 °C for a heating rate of 100 °C h^{-1}. It was thus demonstrated that diffusible hydrogen leaves the sample within 75 h of ageing at ambient temperature.

Cathodic hydrogen charging was carried out for 48 h with a current density of 0.2 mA cm^{-2} in 1 l of 3 wt% NaCl aqueous solution, catalysed with 3 g of NH_4SCN. The specimens were then kept at 20 °C for 100 h to eliminate diffusible hydrogen, leaving only that which is trapped. The samples were then heated to 800 °C at 100 °C h^{-1} in Ar carrier gas, within the chromatograph, to give curves of hydrogen evolution rate versus temperature.

Figure 3 shows the data for Steels A–C. The concentrations represent the hydrogen trapping capacities for each tempering condition. The peak temperature in an evolution rate curve is related to the hydrogen trapping energy (Choo & Lee 1982; Hong & Lee 1983), the 180–200 °C peak corresponding to a trapping energy of about 30 kJ mol^{-1} (Yamasaki *et al.* 1999; Tarui & Yamasaki 2002). It is known that steels with a trapping capacity greater than 3 ppmw have excellent resistance to hydrogen embrittlement

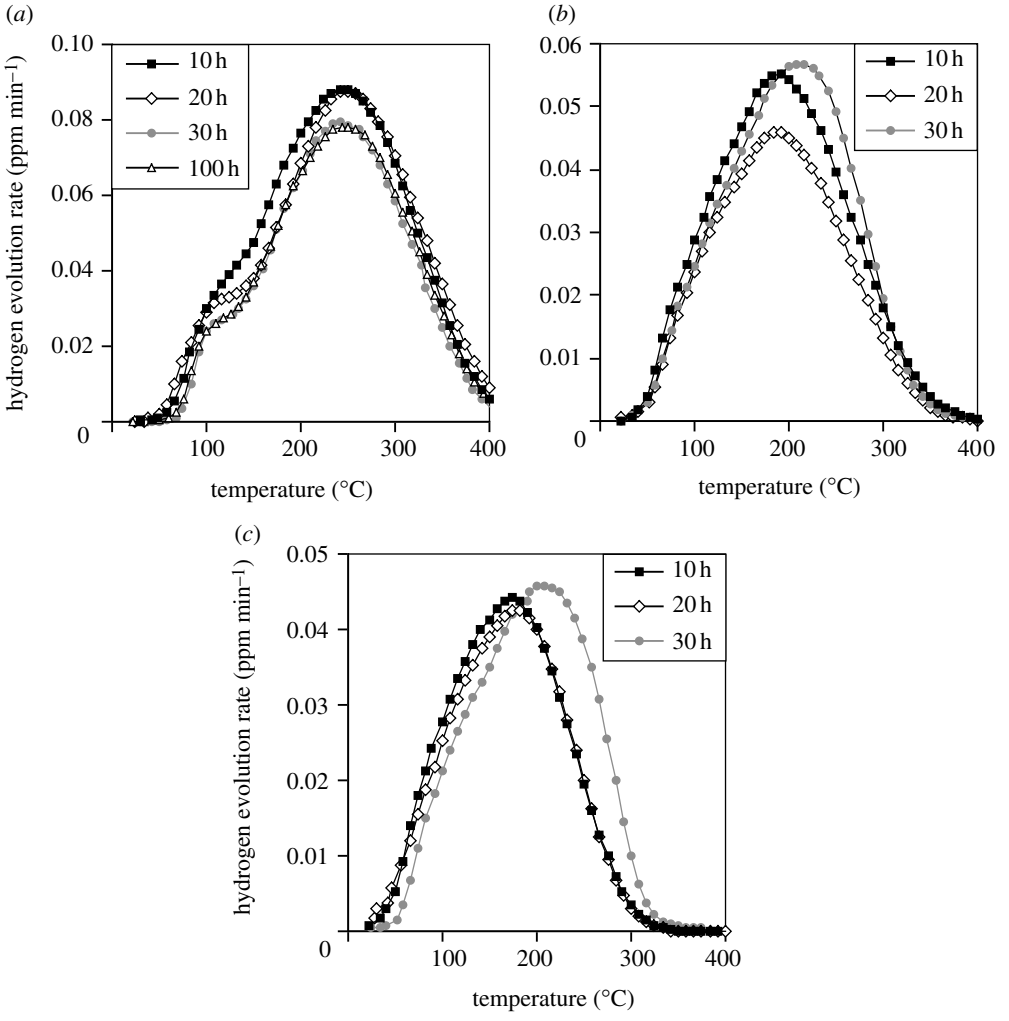

Figure 3. Hydrogen evolution rate: (*a–c*) correspond to Steels A–C, respectively.

(Yamasaki *et al.* 1999; Tarui & Yamasaki 2002). 'ppmw' stands for parts per million by weight.

Figure 4 shows the hydrogen trapping capacity as a function of the tempering time. The amount of trapped hydrogen was obtained by integrating the area under the hydrogen evolution rate curves in figure 3. Data from 0.1C–2.0Mn–0.56V steel are included for comparison (Yamasaki & Bhadeshia 2003). The fact that the trapping capacity peaks with tempering time means that it cannot simply be related to carbide volume and surface area.

3. Modelling growth

The equilibrium phases and their compositions were estimated using MTDATA, allowing cementite, M_2C, M_4C_3, M_7C_3, $M_{23}C_6$, M_6C and ferrite to exist and for all the elements listed in table 1. M_4C_3 and M_6C are predicted to be stable at 600 °C in

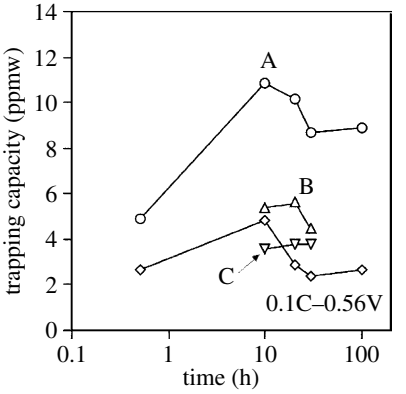

Figure 4. Hydrogen trapping capacity as a function of steel and tempering time at 600 °C.

Steel A with the composition (atomic fraction) of the former being 0.438C–0.440V–0.104Mo–0Mn–0Fe–0.017N and of M_6C, 0.143C–0.048V– 0.500Mo–0Mn–0.310Fe–0N; however, M_6C was not observed using TEM. In Steels B and C, M_4C_3 is predicted to be the only stable carbide with composition 0.444C–0.489V–0.047Mo–0Mn–0Fe–0.019N and 0.450C–0.401V–0.122Mo–0.002Mn–0.000Fe–0.025N, respectively. On the basis of these results, only cementite and M_4C_3 are considered in the calculations.

(*a*) *Capillarity*

Equilibrium is affected by the curvature of the α/β interface. This is the classical Gibbs–Thompson effect, used here for multicomponent alloys as follows.

The simplest exact method to evaluate this capillarity effect in a multicomponent system is to add a term ΔG^{β} to the Gibbs energy of the β phase in the database accessed by MTDATA and to recalculate equilibrium subject to this modification. Consider α, and β in the form of a parabolic cylinder to represent a plate shape. Equilibrium requires that (DeHoff 1993)

$$\mathrm{d}T^{\beta} = \mathrm{d}T^{\alpha} = \mathrm{d}T, \quad \mathrm{d}P^{\beta} = \mathrm{d}P^{\alpha} + \sigma\,\mathrm{d}H \quad \text{and} \quad \mathrm{d}\mu_i^{\beta} = \mathrm{d}\mu_i^{\alpha}, \tag{3.1}$$

where T, P, H, σ and μ represent temperature, pressure, curvature of β phase, interfacial energy per unit area and chemical potential of species i, respectively. Given a constant pressure in α, equation (3.1) gives a pressure change in β due to capillarity as

$$\Delta P = \int_{P(H=0)}^{P} \mathrm{d}P^{\beta} = \int_{H=0}^{H} \sigma\,\mathrm{d}H = \frac{\sigma}{r^{\mathrm{IC}}}, \tag{3.2}$$

where r^{IC} is the radius of curvature at the tip. Accordingly, if v^{β} is the volume per atom of β, the increase in Gibbs energy due to capillarity is ΔG^{β}:

$$\Delta G^{\beta} = \Delta P v^{\beta} = \frac{\sigma v^{\beta}}{r^{\mathrm{IC}}}. \tag{3.3}$$

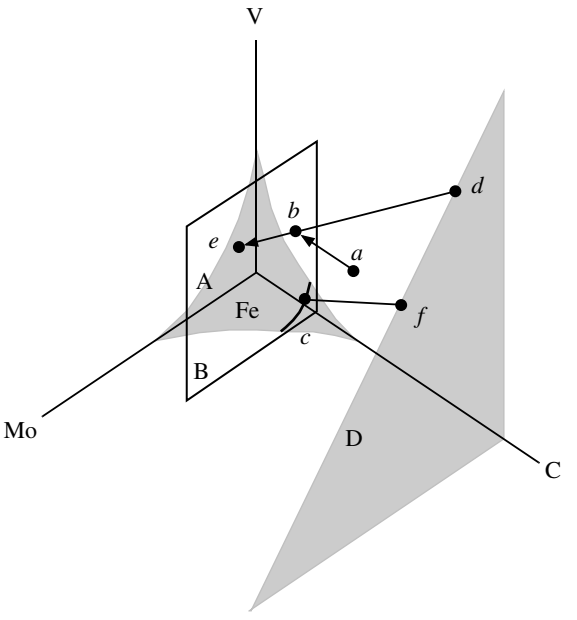

Figure 5. Fe–C–Mo–V phase diagram. The grey surface defines all values of $c^{\alpha\beta}$ (labelled A) and $c^{\beta\alpha}$ (labelled D). The value of $c^{\alpha\beta}$ which allow simultaneous mass-balance for all species must lie on the intersection of the isoconcentration plane B and A.

(*b*) *Growth with local equilibrium and capillarity*

M_4C_3 forms after the paraequilibrium precipitation of cementite and as in previous work (Yamasaki & Bhadeshia 2003), we assume local equilibrium at the M_4C_3/α interface. However, the circumstances are more complicated for the quarternary system considered here, due to the requirement for mass-balance for each component at the interface, even though their mobilities differ. The Péclet numbers, $\bar{p}$, for Mo and V are represented as

$$\bar{p}_{\mathrm{Mo}} = \frac{vr^{\mathrm{IC}}}{2D_{\mathrm{Mo}}} \quad \text{and} \quad \bar{p}_{\mathrm{V}} = \frac{vr^{\mathrm{IC}}}{2D_{\mathrm{V}}}, \tag{3.4}$$

where D_{Mo} and D_{V} are the Mo and V diffusion coefficients in ferrite, v is the precipitate lengthening rate and r^{IC} is the radius of curvature at the plate tip. All species must maintain mass-balance at the interface; focusing first on the substitutional solutes, this requires

$$\bar{p}_{\mathrm{Mo}} D_{\mathrm{Mo}} = \bar{p}_{\mathrm{V}} D_{\mathrm{V}}. \tag{3.5}$$

Trivedi's (1970) solution for the lengthening of parabolic cylinders (plates) allows the composition to vary along the curved interface, but it is limited to large values of supersaturation (Yamasaki & Bhadeshia 2003). Therefore, an alternative approach due to Bolling & Tiller (1961) was adopted. This retains the parabolic cylinder shape with an assumed constant concentration over its surface, at a value appropriate to the tip radius. For diffusion-controlled growth,

the Péclet numbers, $\bar{p}_{\mathrm{Mo}}$ and $\bar{p}_{\mathrm{V}}$, must simultaneous satisfy (Christian 1975*a*)

$$\Omega_{\mathrm{Mo}}\left(1-\frac{r_{\mathrm{c}}}{r^{\mathrm{IC}}}\right)=\sqrt{\pi\bar{p}_{\mathrm{Mo}}}\exp(\bar{p}_{\mathrm{Mo}})\mathrm{erfc}(\sqrt{\bar{p}_{\mathrm{Mo}}}), \tag{3.6}$$

$$\Omega_{\mathrm{V}}\left(1-\frac{r_{\mathrm{c}}}{r^{\mathrm{IC}}}\right)=\sqrt{\pi\bar{p}_{\mathrm{V}}}\exp(\bar{p}_{\mathrm{V}})\mathrm{erfc}(\sqrt{\bar{p}_{\mathrm{V}}}), \tag{3.7}$$

where the supersaturation $\Omega_i=(\bar{c}_i-c_i^{\alpha\beta})/(c_i^{\beta\alpha}-c_i^{\alpha\beta})$. Here, $\bar{c}_i$ is the atom fraction of i in ferrite at the point where precipitation begins, $c_i^{\alpha\beta}$ is the atom fraction of i in ferrite which is in equilibrium with β (M_4C_3) and $c_i^{\beta\alpha}$ is similarly interpreted. r_{c} is the critical tip radius at which growth ceases.

Local equilibrium must also be maintained for interstitial carbon, which diffuses many orders of magnitude faster than the substitutional atoms. We follow the method of Coates (1972), where a tie-line is selected such that the substitutional solute flux can keep up with carbon by reducing its concentration gradient. In the quarternary phase diagram of figure 5, b is the matrix composition from which M_4C_3 precipitates, $c^{\alpha\beta}$ is designated c and ($c^{\beta\alpha}$) is f. The point a is the alloy composition from which paraequilibrium cementite precipitates; e and d are ends of the tie-line which passes through b. Since $D_{\mathrm{Mo}}\ll D_{\mathrm{C}}$ and $D_{\mathrm{V}}\ll D_{\mathrm{C}}$, $c^{\alpha\beta}$ will lie on the intersection of plane B which passes through b, with the surface A defining all possible values of $c^{\alpha\beta}$.

For a given value of r^{IC}, the curve representing $c^{\alpha\beta}$ on B is uniquely determined; c can be any point on this curve, connected by a tie-line to f on the $c^{\beta\alpha}$ surface. There are therefore many choices for the tie-line determining interface compositions but only one can simultaneously satisfy mass-balance for all solutes, thus yielding the Péclet number. However, the velocity (lengthening rate) depends on the tip radius. It is assumed that the tip radius adopted is that which gives the maximum velocity $v_{\max}$.

(*c*) *Enrichment and dissolution of cementite*

Cementite is the first to precipitate during the tempering of martensite in the steels studied here. In *paraequilibrium* transformation, the substitutional solute to iron atom ratio of the parent and product phases is preserved, while the more mobile carbon achieves a uniform chemical potential subject to that constraint (Hultgren 1968). The cementite that forms during the tempering of martensite grows by a paraequilibrium, displacive mechanism (Bhadeshia 1989, 2001; Takahashi & Bhadeshia 1990; Babu *et al.* 1993; Thomson & Miller 1995, 1998). The partitioning of elements, such as manganese, vanadium, molybdenum, does not therefore occur during its precipitation, leaving it with a chemical composition which is not at equilibrium with the matrix. During tempering, this composition tends towards equilibrium, resulting in an enrichment of Mo and V within the cementite.

The rate of enrichment is given by (Bhadeshia 1989)

$$c_{\mathrm{M}}^{\theta}\simeq\bar{c}_{\mathrm{M}}+4\sqrt{D_{\mathrm{M}}t}\,\frac{(\bar{c}_{\mathrm{M}}-c_{\mathrm{M}}^{\alpha\theta})}{d_{\mathrm{t}}\sqrt{\pi}}, \tag{3.8}$$

where c_{M}^{θ} represents the atomic fraction of solute M in cementite, t is the time since cementite formation, d_{t} is the thickness of the cementite plates, D_{M} is the

diffusion coefficient of solute M in the matrix, $c_{\mathrm{M}}^{\alpha\theta}$ is the atomic fraction of the substitutional solute in the ferrite which is in local equilibrium with the cementite, and $\bar{c}_{\mathrm{M}}$ is the mean atomic fraction of solute M in the alloy. The average thickness of cementite plates was measured, using TEM, to be approximately 2×10^{-8} m in the grains and 5×10^{-8} m on the grain boundaries.

The dissolution rate v_θ is given by (Robson & Bhadeshia 1997)

$$v_\theta = -\frac{D_{\mathrm{M}}}{\bar{d}}\,\frac{c_{\mathrm{M}}^{\alpha\theta} - c_{\mathrm{M}}^{\alpha\mathrm{M_4C_3}}}{c_{\mathrm{M}}^{\theta\alpha} - c_{\mathrm{M}}^{\alpha\theta}}, \tag{3.9}$$

where D_{M} is the diffusion coefficient of the slowest diffuser M, which is molybdenum in Fe–C–Mo–V systems, and $\bar{d}$ is the mean diffusion distance between θ and M_4C_3 precipitates,

$$\bar{d} = (N^\theta + N^{\mathrm{M_4C_3}})^{-(1/3)}, \tag{3.10}$$

where N^θ and $N^{\mathrm{M_4C_3}}$ are the number densities of θ and M_4C_3, respectively.

(i) *Nucleation of* M_4C_3

Following classical theory, the nucleation rate is

$$I = N\frac{kT}{h}\exp\left\{\frac{-(G^* + Q^*)}{kT}\right\} \quad \text{with} \quad G^* = \frac{16\pi}{3}\,\frac{\sigma^3}{\Delta G_{\mathrm{V}}^2}, \tag{3.11}$$

where N is the number of nucleation sites per unit volume of the system, Q^* is the activation energy for the transfer of atoms across the interface (approximately equal to that for self-diffusion of iron, given that the interface is likely to be coherent at nucleation), k is the Boltzmann constant and h is the Planck constant (Christian 1975*a*,*b*). G^* is the activation energy for nucleation and ΔG_{V} is the chemical free energy change per unit volume of nuclei. ΔG_{V} for M_4C_3 is calculated using MTDATA as -2.440×10^9 J m^{-3} for the beginning of precipitation, but its magnitude diminishes during the course of the reaction. The method for calculating the growth rate has already been described.

(ii) *Coarsening*

Coarsening is driven by differences in the curvature of the interfaces of particles of different size; the larger particles then grow at the expense of the smaller ones with sharper curvatures. For coarsening, M_4C_3 particles were modelled as plates as illustrated in figure 6. The growth (or dissolution) rate can be estimated according to Zener (1946) by

$$v \simeq \frac{D_{\mathrm{M}}}{d}\,\frac{C_{\mathrm{M}}^{\mathrm{M_4C_3}\alpha} - c_{\mathrm{M,r}}^{\alpha\mathrm{M_4C_3}}}{\bar{c}_{\mathrm{M}} - c_{\mathrm{M,r}}^{\alpha\mathrm{M_4C_3}}}, \tag{3.12}$$

where $c_{\mathrm{M,r}}^{\alpha\mathrm{M_4C_3}}$ is the equilibrium concentration of solute M in ferrite at the curved interface and $\bar{d}$ is the mean diffusion distance between particles:

$$\bar{d} = (N^\beta)^{-(1/3)}, \tag{3.13}$$

where N^β is the number density of M_4C_3 particles.

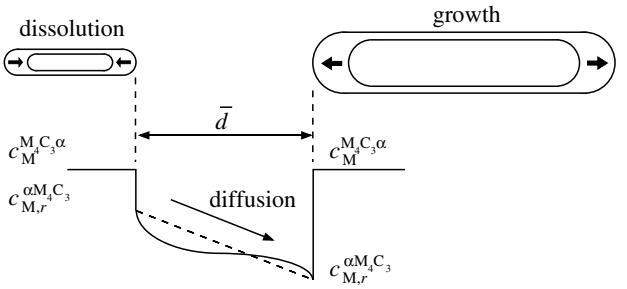

Figure 6. Coarsening of disc-shaped particles.

Modelling of coarsening in a quaternary system has the same requirements as precipitation, to satisfy the mass-balance at the interface for all solutes. However, adopting Zener's maximum growth rate hypothesis and using the approach explained in figure 5, it is possible to obtain a unique growth or dissolution rate for each size of M_4C_3 particle.

Our treatment of coarsening is approximate since the plate shape is retained, whereas it is possible that the particles might spheroidize. This might be justified by the observation that the plate aspect ratio does not seem to change significantly from 6 during the heat treatments used.

(iii) *Calculation sequence and parameters*

The calculations covering precipitation were performed in time-steps of 50 s, with the nucleation and lengthening rates, the number density of nucleation sites remaining, the solute concentrations in the matrix and the enrichment and dissolution of cementite updated in each step.

The parameters used in the calculations are listed in table 2. The nucleation site density was obtained by fitting with experimental data. The M_4C_3/ferrite interface energy is from Porter & Easterling (1992), the diffusivity of vanadium in ferrite from Bowen & Leak (1970) and that of molybdenum from Heijwegen & Rieck (1974).

4. Results and discussion

Figure 7 compares calculated and measured data; the solid circles represent the average of data from different areas, with scatter in the results indicated by the error bars. The calculations are consistent with the observations. There have been attempts to characterize vanadium carbide, e.g. the lattice structure (Baker & Nutting 1959; Tanino & Nishida 1965; Ustinovshchikov 1984), morphology (Tanino & Nishida 1965; Ustinovshchikov 1984; Hara *et al.* 2001), average size (Dunlop & Honeycombe 1978; Hara *et al.* 2001) and size distribution (Dunlop & Honeycombe 1978) but variations as a function of tempering time, for both the precipitation and coarsening stages, have not been reported previously.

The carbon content of the ferrite is minimal (approximately equal to 0.022 at.% using MTDATA) once cementite has precipitated. The source of carbon for the subsequent formation of M_4C_3 is from the dissolution of cementite, as illustrated in figure 7*a*. After the completion of precipitation, coarsening

Table 2. The calculation parameters.

parameter	Steel A	Steel B	Steel C
shape	plate	plate	plate
tempering temperature (°C)	600	600	600
surface energy of M_4C_3 (J m^{-2})	0.2	0.2	0.2
driving force for nucleation (J m^{-3})	-2.440×10^{9}	-2.064×10^{9}	-2.064×10^{9}
nucleation site density (m^{-3})	1.48×10^{22}	1.48×10^{22}	1.48×10^{22}
maximum volume fraction of cementite	1.796×10^{-2}	1.796×10^{-2}	1.796×10^{-2}
maximum volume fraction of M_4C_3	9.73×10^{-3}	9.73×10^{-3}	9.73×10^{-3}
$c_{\mathrm{V}}^{\alpha\theta}$ (atomic fraction)	4.4911×10^{-3}	4.3056×10^{-3}	2.1462×10^{-3}
$c_{\mathrm{Mo}}^{\alpha\theta}$ (atomic fraction)	8.9045×10^{-3}	7.4201×10^{-3}	2.2048×10^{-3}
$c_{\mathrm{V}}^{\theta\alpha}$ (atomic fraction)	1.009×10^{-1}	1.035027×10^{-1}	6.42492×10^{-2}
$c_{\mathrm{Mo}}^{\theta\alpha}$ (atomic fraction)	2.907×10^{-2}	7.4201×10^{-3}	8.643×10^{-3}
$c_{\mathrm{V}}^{\alpha\mathrm{M_4C_3}}$ (atomic fraction)	1.845×10^{-3}	1.2894×10^{-3}	2.90×10^{-5}
$c_{\mathrm{Mo}}^{\alpha\mathrm{M_4C_3}}$ (atomic fraction)	8.1739×10^{-3}	1.7848×10^{-3}	6.567×10^{-4}
$c_{\mathrm{V}}^{\mathrm{M_4C_3}\alpha}$ (atomic fraction)	4.313452×10^{-1}	4.825583×10^{-1}	3.410878×10^{-1}
$c_{\mathrm{Mo}}^{\mathrm{M_4C_3}\alpha}$ (atomic fraction)	1.152479×10^{-1}	5.5268×10^{-2}	1.753835×10^{-1}
thickness of cementite in grains (m)	2.0×10^{-8}	2.0×10^{-8}	2.0×10^{-8}
thickness of cementite on grain boundaries (m)	5.0×10^{-8}	5.0×10^{-8}	5.0×10^{-8}
diffusion constant of V, D_{V} (m^2 s^{-1})	3.05×10^{-4}	3.05×10^{-4}	3.05×10^{-4}
diffusion constant of Mo, D_{Mo} (m^2 s^{-1})	2.29×10^{-4}	2.29×10^{-4}	2.29×10^{-4}
activation energy for V diffusion, Q_{V} (J mol^{-1})	2.39×10^{5}	2.39×10^{5}	2.39×10^{5}
activation energy for Mo diffusion, Q_{Mo} (J mol^{-1})	2.39×10^{5}	2.39×10^{5}	2.39×10^{5}

occurs with insignificant changes in the fraction of M_4C_3 (figure 7). As a rough statement, in Steel A, the fraction of M_4C_3 increases for 30 h to be followed by coarsening. The lengths of all M_4C_3 particles increase during precipitation; although the *mean* length increases during coarsening, the smaller particles dissolve.

The calculated number density of M_4C_3 particles longer than 4 nm is shown in figure 7*c* for comparison with observations, since particles less than that size could not readily be characterized using microscopy. The number clearly decreases during coarsening. In the 30 h distribution illustrated in figure 7*d*, a bin size of X corresponds to lengths in the range (X−2.5) to (X+2.5) nm.

In a multicomponent system, the tie-line determining local equilibrium at the interface is not necessarily that corresponding to the ultimate equilibrium state. This follows from the requirement for simultaneous mass-balance for all solutes, even though they may diffuse at vastly different rates. The consequence is that the composition of the precipitate changes during the course of isothermal treatment. This is why the Mo concentration of M_4C_3 in Steel A is higher during growth than the ultimate equilibrium concentration. Figure 7*e* compares the evolution of the measured and calculated compositions of M_4C_3 as a function of tempering time.

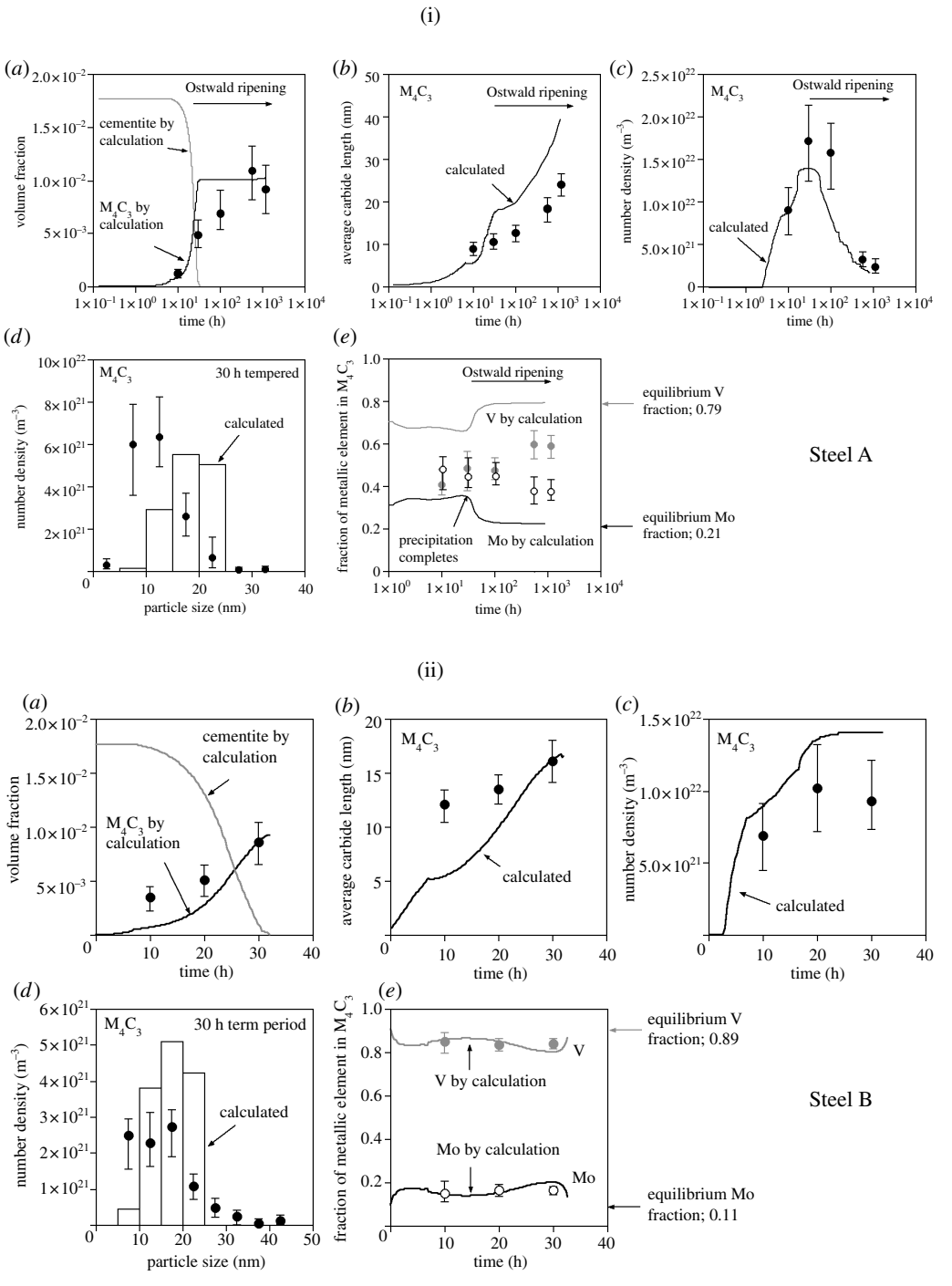

Figure 7. Calculated and measured data for M_4C_3. (*a*) Volume fraction. (*b*) Average length. (*c*) Number density. (*d*) Length distribution after 30 h tempering. (*e*) Chemical composition.

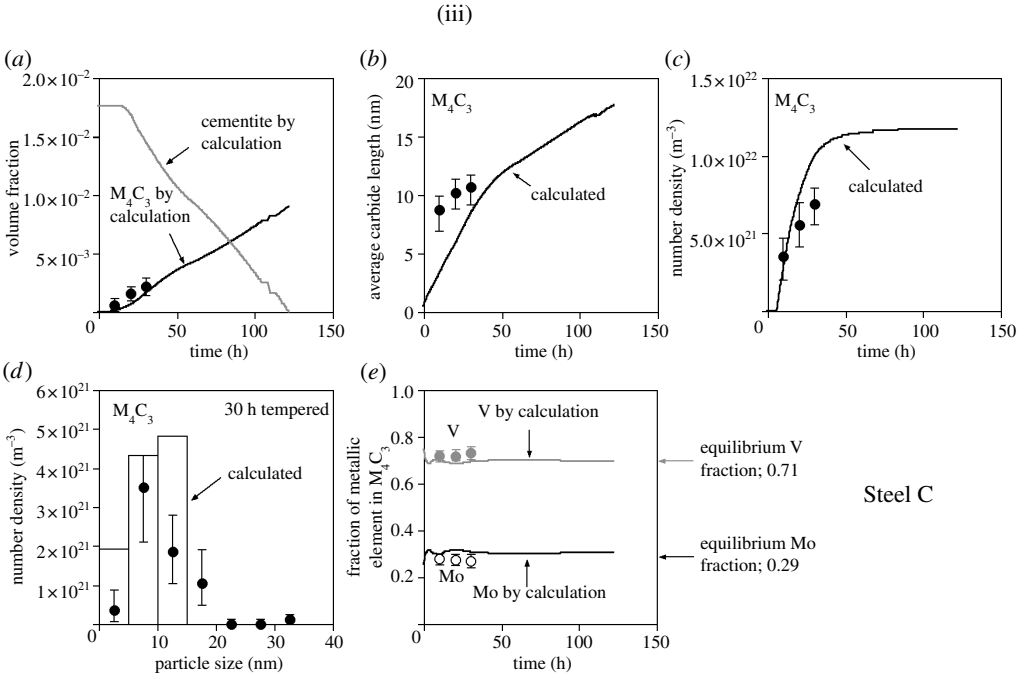

Figure 7. (*Continued.*)

The crystallographic orientation between M_4C_3 and ferrite is (Baker & Nutting 1959; Tekin & Kelly 1965)

$$\{100\}_{M_4C_3} \| \{100\}_\alpha, \langle 100\rangle_{M_4C_3} \| \langle 110\rangle_\alpha. \tag{4.1}$$

M_4C_3 plates have a misfit of only 2.1% on $\{100\}_\alpha$, but 47% normal to that plane (Tanino 1988). This is why M_4C_3 grows as a thin plate on $\{100\}_\alpha$. A corollary is that spheroidizing must lead to a breakdown of coherency and an increase in the surface energy, and hence may not be favoured.

Given that vanadium forms hydrides, the V–H interaction is expected to be strong. However, chemical interactions between solutes and hydrogen cannot explain the carbide size dependence of the trapping capacity; although the average size and fraction of M_4C_3 particles increases monotonically with the tempering time, the trapping capacity peaks at 10 h, where the mean particle-length is about 10 nm (figure 7). Coincidentally, the contribution made by precipitation hardening, derived by removing the base-steel hardness from the actual hardness (figure 2), also peaks at about 10 h of tempering time (figure 8). Coherency strains are expected to be greatest at peak hardening.

There is another important factor which controls the hydrogen trapping: the fraction of Mo amongst metallic elements in M_4C_3 particles. Figure 9 shows the hydrogen trapping capacity per M_4C_3 particle, obtained by dividing the trapping capacity with the number density of M_4C_3 particles at 10 h tempering and the metallic fraction of Mo in M_4C_3. The trapping capacity is greater at larger Mo fractions. It is known that the lattice parameter of M_4C_3 increases with its Mo fraction (Novotny & Kieffer 1949), which must influence its coherency with the

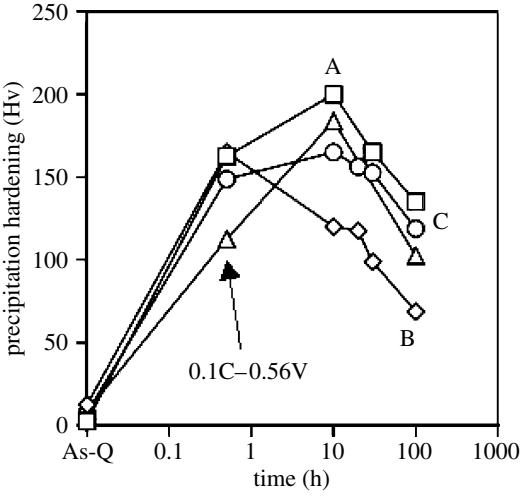

Figure 8. Relationships between the contribution of precipitation hardening to the total hardness, and tempering time at 600 °C.

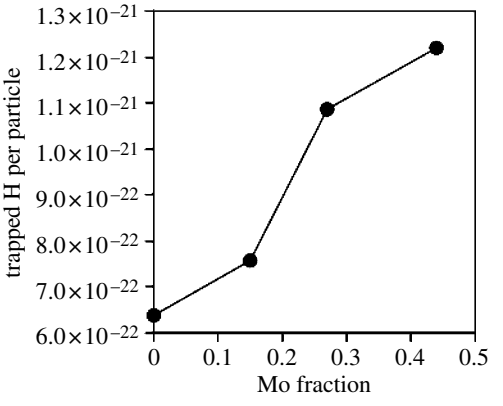

Figure 9. Hydrogen trapping capacity per M_4C_3 particle versus fraction of Mo in 'M' of M_4C_3.

ferrite, and hence the hydrogen trapping capacity via the elastic interaction of the coherency strains with the hydrogen atoms.

It is useful to discuss how the model might be used to develop better steels in the context of hydrogen embrittlement. The heat treatment of such steels (tempering time and temperature) is not a free variable, but is determined from the independent need to simultaneously optimize strength, toughness and other engineering parameters. The present work has shown that for the steels considered, the most effective size of M_4C_3 particles for hydrogen trapping is about 10 nm. Furthermore, for a given size, the state of coherency of the carbide is optimum when it contains a large molybdenum concentration. The mathematical model can in principle be used to estimate the alloy composition, which would lead to the correct carbide size and molybdenum content for a given

heat treatment. A more quantitative treatment of trapping depends on the development of theory for the state of coherency of M_4C_3, together with a model for the interactions between dissolved hydrogen and the coherency strains.

5. Conclusions

The main conclusion of this work, other than the development of theory capable of modelling precipitation behaviour, is that the hydrogen trapping capacity of a steel is not simply dependent on the number density of precipitates. It has been demonstrated that the precipitate coherency strains and their interaction with hydrogen influence the hydrogen trapping capacity. This in turn means that there is an advantage in using multicomponent carbides to develop hydrogen-resistant steels whose chemical composition can be manipulated to adjust their state of coherency with the ferrite matrix.

The authors are grateful to the Nippon Steel Corporation for funding this work and to the University of Cambridge for the provision of laboratory facilities. The Department of Materials Science and Metallurgy can be found on the web at http://www.msm.cam.ac.uk/phase-trans.

References

Ashai, H., Hirakami, D. & Yamasaki, S. 2002 *ISIJ Int.* **43**, 527–533.
Babu, S. S., Hono, K. & Sakuri, T. 1993 *Metall. Trans. A* **67**, 321–327.
Baker, R. G., & Nutting, J. 1959 *ISI Special Report No. 64*, pp. 1–22. London: The Iron and Steel Institute.
Bhadeshia, H. K. D. H. 1989 *Mater. Sci. Technol.* **5**, 131–137.
Bhadeshia, H. K. D. H. 2001 *Bainite in steels*, p. 63. London: Institute of Materials.
Bollling, G. F. & Tiller, W. A. 1961 *J. Appl. Phys.* **32**, 2587–2605. (doi:10.1063/1.1728359)
Bowen, A. W. & Leak, G. M. 1970 *Metall. Trans.* **1**, 1695–1700.
Choo, W. Y. & Lee, J. Y. 1982 *J. Mater. Sci.* **17**, 1930–1938. (doi:10.1007/BF00540409)
Christian, J. W. 1975*a* *Theory of transformations in metals and alloys. Part 1*, p. 498, 2nd edn. Oxford: Pergamon Press.
Christian, J. W. 1975*b* *Theory of transformations in metals and alloys. Part 1*, p. 441, 2nd edn. Oxford: Pergamon Press.
Coates, D. E. 1972 *Metall. Trans.* **3**, 1203–1212.
DeHoff, R. T. 1993 *Thermodynamics in materials science*, p. 378. New York: McGraw-Hill.
Dunlop, G. L. & Honeycombe, R. W. K. 1978 *Metal Sci.* **12**, 367–371. (doi:10.1016/0036-9748(78)90301-0)
Gladman, T. 1997 *The physical metallurgy of microalloyed steels*, pp. 1–362. London: Institute of Materials.
Hack, K. (ed.) 1996. *Thermodynamics at work*. London: Institute of Materials.
Hara, T., Tsuchida, T. & Tsuzaki, K. 2001 *CAMP-ISIJ* **14**, 641.
Heijwegen, C. P. & Rieck, G. D. 1974 *Acta Metall.* **22**, 1268–1281.
Honeycombe, R. W. K. & Bhadeshia, H. K. D. H. 1995*a* *Steels, microstructure and properties*, pp. 1–364. London: Edward Arnold.
Honeycombe, R. W. K. & Bhadeshia, H. K. D. H. 1995*b* *Steels*, pp.181–199, 2nd edn. London: Edward Arnold.
Hong, G. W. & Lee, J. A. 1983 *J. Mater. Sci.* **18**, 271–277. (doi:10.1007/BF00543835)
Hultgren, A. 1968 *Trans. ASM* **39**, 915–1005.
Ibaraki, N., Inada, A., Shimotsusa, M. & Nagao, M. 1998 *Kobelco Technol. Rev.* **21**, 21–25.
Kelly, P. M. & Nutting, J. 1959 *J. Iron Steel Inst.* **191**, 246–248.

Kosaka, M., Yoshida, S. & Tarui, T. 2004 *CAMP-ISIJ* **17**, 1370.
Kushida, T., Kuratomi, N., Kudoh, T., Matumoto, H., Tsumura, T. & Nakasato, F. 1996 *Testu-to-Hagane* **82**, 297–302.
Nowotny, H. & Kieffer, R. 1949 *Z. Metallkd.* **38**, 257.
NPL 2004 *MTDATA software*. Teddington: National Physical Laboratory.
Porter, D. A. & Easterling, K. E. 1992 *Phase transformations in metals and alloys*, p. 147, 2nd edn. London: Chapman & Hall.
Robson, J. D. & Bhadeshia, H. K. D. H. 1997 *Mater. Sci. Technol.* **13**, 631–639.
Takahashi, M. & Bhadeshia, H. K. D. H. 1990 *Mater. Sci. Technol.* **6**, 592–603.
Tanino, M. 1988 *Proc. Int. Conf. on Phys. Metall. Thermomech. Processing of Steels and other Metals, Montreal*, vol. 1, pp. 70–79.
Tanino, M. & Nishida, T. 1965 *J. Jpn Inst. Met.* **29**, 794–800.
Tarui, T. & Yamasaki, S. 2002 *Testu-to-Hagane* **88**, 612–619.
Tekin, E. & Kelly, P. M. 1965 *J. Iron Steel Inst.* **203**, 715–720.
Thomson, R. C. & Miller, M. K. 1995 *Appl. Surf. Sci.* **87/88**, 185–193. (doi:10.1016/0169-4332(94)00496-X)
Thomson, R. C. & Miller, M. K. 1998 *Acta Metall.* **46**, 2203–2213.
Trivedi, R. 1970 *Metall. Trans.* **1**, 921–927.
Ustinovshchikov, Y. I. 1984 *Metal Sci.* **18**, 337–344. (doi:10.1016/0036-9748(84)90448-4)
Yamasaki, S. & Bhadeshia, H. K. D. H. 2003 *Mater. Sci. Technol.* **19**, 1335–1343. (doi:10.1179/026708303225005971)
Yamasaki, S., Kubota, M. & Tarui, T. 1999 *Nippon Steel Tech. Rep.* **80**, 50–55.
Zener, C. 1946 *Trans. AIME* **167**, 550–595.